



The fabrication of bio-renewable and recyclable cellulose based carbon microspheres incorporated by CoFe_2O_4 and the photocatalytic properties

Lu Gan ^{a,1}, Aobo Geng ^{a,1}, Lijie Xu ^b, Meijuan Chen ^c, Liangcai Wang ^a, Jie Liu ^d, Shuguang Han ^a, Changtong Mei ^{a,*}, Qiang Zhong ^a

^a College of Materials Science and Engineering, Nanjing Forestry University, Nanjing, 210037 Jiangsu, People's Republic of China

^b College of Biology and the Environment, Nanjing Forestry University, Nanjing, 210037 Jiangsu, People's Republic of China

^c School of Human Settlements and Civil Engineering, Xi'an Jiaotong University, Xi'an, 710049 Shaanxi, China

^d School of Chemical Biology and Materials Engineering, Suzhou University of Science and Technology, Suzhou, 215009 Jiangsu, People's Republic of China

ARTICLE INFO

Article history:

Received 27 January 2018

Received in revised form

8 June 2018

Accepted 9 June 2018

Available online 11 June 2018

Keywords:

Cellulose

Carbon microsphere

Ferromagnetic recyclable

Photocatalyst

Pollutant degradation

ABSTRACT

The bio-renewable cellulose based carbon microspheres through a one-step hydrothermal process (CMS) and a two-step hydrothermal plus pyrolysis process (pCMS) were prepared in the present study, respectively. The prepared carbon microspheres were then hybridized with magnetic CoFe_2O_4 to prepare recyclable photocatalyst composites. The impact of pyrolysis step on the photocatalysis performance of the composites were then investigated through degrading rhodamine B dye. The results indicated that the incorporation of both CMS and pCMS could significantly enhance the photocatalytic efficiency of the pristine CoFe_2O_4 . Since the pyrolysis carbonization process led to a higher graphitization degree to the pCMS, the pCMS- CoFe_2O_4 exhibited higher photocatalytic properties than the CMS- CoFe_2O_4 . Moreover, due to the existence of the magnetic CoFe_2O_4 , the prepared photocatalysts could be easily separated from the water and readily reused for more cycles, achieving the goal of cleaner production through avoiding secondary pollution lead by the photocatalyst. The present study could open up a new thinking of preparing environmentally sustainable photocatalyst using bio-renewable biomass in the field of wastewater treatment.

© 2018 Elsevier Ltd. All rights reserved.

1. Introduction

Photocatalysis technology has attracted enormous research interest recently in solving water contamination problems, especially the degradation of organic pollutants due to its merits of high efficiency, high reaction rate, low toxicity, etc. (Dhiman et al., 2017; Gan et al., 2016a, 2016b; Reddy et al., 2011). Moreover, the photocatalysis technology has been thought as an environment-friendly wastewater treatment approach since it utilizes light source as the energy (Ananpattarachai and Kajitvichyanukul, 2016). During the photocatalytic process, the photocatalysts harness the photo energy from the irradiation light to form electron-hole pairs, and produce active radicals which will further drive chemical reactions

to decompose organic pollutants (Hadnadjev-Kostic et al., 2017; Xu et al., 2017). In the past few decades, many semiconductors, such as TiO_2 , ZnS and CdS, which demonstrated efficient photocatalytic properties, have been well investigated (Meng et al., 2013; Pozo-Antonio and Dionísio, 2017; Reddy et al., 2015, 2016). However, on account of the limitation of wide band gaps, say normally higher than 3.0 eV, these semiconductors can only absorb UV range light, resulting in a relatively low potency in utilization of solar energy (Achouri et al., 2016; Ahmad et al., 2013). Thus, numerous studies have been conducted to develop high-efficient photocatalysts with narrower band gaps which could effectively utilize the incident light and generate redox reactions (Ao et al., 2014; Priyadharsan et al., 2017).

Amongst them, the ferromagnetic photocatalysts, which are chemically and thermally stable magnetic materials, have been studied intensively since they provide desirable optical absorption with relatively narrow band gaps (~2 eV) (Choi et al., 2015; Gan et al., 2015a; Reddy et al., 2008a). Moreover, desirable magnetic

* Corresponding author.

E-mail address: mei@njfu.edu.cn (C. Mei).

¹ These authors contributed equally to this work.

properties can also be provided by the ferromagnetic photocatalysts, which facilitate easy separation from wastewater by magnetic field, and achieves the goal of cleaner production through avoiding secondary pollution to the natural water bodies (Della Pina et al., 2015). Besides, the separated photocatalysts can be recycled for further use, which can be considered as environmentally sustainable materials for wastewater treatment. Thus, the ferromagnetic photocatalyst is considered as a promising alternative to the traditionally used UV-activated catalysts. Meanwhile, it has also been found in many studies that the combination of carbonaceous materials and photocatalysts could simultaneously reduce the band gap and decrease the recombination rate of electron and hole pairs of the photocatalysts, resulting in a higher photo energy conversion rate (Fu et al., 2012; Hassan et al., 2014; Hu et al., 2015). However, most of these carbonaceous materials, such as graphene, carbon nanofibers, are mainly derived from the gradually declining oil resources (Reddy et al., 2008b, 2014), which will induce energy crisis in the long term. Recent studies have shown that being pyrolyzed at oxygen-limited conditions, the naturally abundant biomass could be turned to carbon-enriched biochar materials, and these biomass derived carbonaceous materials could serve as desirable carbon alternatives (Dunnigan et al., 2018; Pi et al., 2015). As a representative, the cellulose is a natural biomass with the advantages of being abundant, ecofriendly, cheap, sustainable and renewable (Laadila et al., 2017; Wan et al., 2015). It has been shown that after hydrothermal process integrated with pyrolysis treatment, the cellulose based carbon microspheres with high specific surface areas, large pore size and low densities could be fabricated (Wu et al., 2015a, 2015b). Previous studies also have indicated that semiconductors loaded microsphere photocatalysts showed enhanced photocatalytic properties since high specific surface areas and large pore size of the microspheres could facilitate the adsorption of organic pollutants, which could improve accelerate the following photo-degradation process (Wang et al., 2017). However, limited studies have investigated the photocatalytic properties of the cellulose carbon microsphere based composite photocatalysts. Furthermore, few studies have discussed the recovery and recycling of these microsphere based photocatalysts until recently.

Herein, two kinds of carbon microspheres were prepared using a one-step hydrothermal process (CMS) and a two-step hydrothermal plus pyrolysis (pCMS) process. The prepared CMS and pCMS were further hybridized with the ferromagnetic cobalt ferrite (CoFe_2O_4) to prepare the photocatalyst composites. The structure and morphology of the prepared composites were then investigated in detail. Afterwards, the photo-degradation performance of the prepared composites were examined through degrading rhodamine B (RhB) dye. Specifically, the impact of CMS and pCMS on the photo-degradation efficiency of the composites were studied in detail. Finally, a mechanism was also proposed subsequently. To realize cleaner production, the objectives of this study are to provide application potentials of biorenewable biomass derived carbon materials in wastewater treatment, and to prepare magnetic recyclable photocatalyst which could be reused for cycles for the degradation of organic pollutants.

2. Experimental

2.1. Materials

Sodium carboxymethylcellulose (CMC), ferric nitrate nonahydrate ($\text{Fe}(\text{NO}_3)_3 \cdot 9\text{H}_2\text{O}$) and cobalt nitrate hexahydrate ($\text{Co}(\text{NO}_3)_2 \cdot 6\text{H}_2\text{O}$) were purchased from Sigma (USA). Rhodamine B dye (RhB) was purchased from Nanjing Chemical Reagent Co., Ltd. (China). Commercial Degussa P25 was purchased from Beijing Yonge Water Biological Technology Co., Ltd. (China). Other

chemicals and solvents were all of analytical grade and used as received (Nanjing Chemical Reagent Co., Ltd., China). Distilled water was used exclusively in this study.

2.2. Preparation of the CMS and pCMS

In a typical experiment, CMC (1.5 g) was first dissolved in distilled water (40 mL). The clear CMC solution was then transferred into a Teflon autoclave, which was heated in the oven at 210°C for 12 h. The resultant solid was washed with water and ethanol for three times, respectively. After being dried at 60°C for 12 h, the CMS was obtained. Then the CMS was pyrolyzed at 800°C for 4 h under nitrogen atmosphere, and the p-CMS was obtained.

2.3. Preparation of the CMS- CoFe_2O_4 and pCMS- CoFe_2O_4 composites

The CMS- CoFe_2O_4 and pCMS- CoFe_2O_4 composites were prepared using a coprecipitation method mentioned as follows. Based on the previous studies, the amount of carbon microspheres was set at ~20 wt% (Fu et al., 2012; Gan et al., 2015a). Typically, 4.0 g of $\text{Fe}(\text{NO}_3)_3 \cdot 9\text{H}_2\text{O}$ (10 mmol) and 1.5 g of $\text{Co}(\text{NO}_3)_2 \cdot 6\text{H}_2\text{O}$ (5 mmol) were added into 20 mL of distilled water. After all the solids were dissolved, 200 mg of CMS or pCMS was added into the solution. The mixture was further sonicated for ~2 h under ambient temperature before NaOH solution (1 M) was added dropwise to adjust the pH of the solution to ~10.0 under continuous mechanical stirring. After being mechanically stirred for another 1 h, the mixture was put into a Teflon-lined autoclave and kept at 180°C for 12 h. The precipitate was then washed with 2×50 mL of distilled water, 2×50 mL of ethanol and 2×50 mL of acetone, respectively. After being dried at 80°C for 24 h, the as-prepared CMS- CoFe_2O_4 and pCMS- CoFe_2O_4 composites were finally obtained. For comparison, pure CoFe_2O_4 without the introduction of CMS and pCMS were also prepared following similar procedures. The preparation steps were illustrated in Fig. 1.

2.4. Characterizations

Fourier transform infrared (FT-IR) spectra were recorded by a Perkin Elmer 100 spectrophotometer at wavenumbers ranging from 4000 to 450 cm^{-1} with a resolution of 4 cm^{-1} and 16 scans. The X-ray diffraction (XRD) was conducted using a Rigaku Smartlab XRD instrument with the $\text{Cu-K}\alpha$ as the radiation source (1.54 Å). Raman spectra were performed using a Thermo DXR532 Raman spectrometer, which was equipped with an Ar laser (532 nm, 180 mW) as the excitation light source, and a microscope. The morphology of the prepared composites was observed by scanning electron microscopy (SEM) using the FEI Quanta 200 equipped with energy dispersive spectroscopy (EDS). Nitrogen adsorption/desorption isotherms at 77 K were performed with a Quantachrome v3.0 instrument, and the data was analyzed by a multipoint Brunauer–Emmett–Teller (BET) method. The diffuse reflectance spectra (DRS) were conducted by a Perkin Elmer Lambda 950 UV/Vis/NIR spectrophotometer. The photoluminescence (PL) spectra of the microspheres were conducted by Perkin-Elmer LS55 spectrofluorometer with a Xe Lamp as the excitation source. The excitation wavelength was selected as 350 nm. The magnetic measurement was conducted with a Quantum Design vibrating sample magnetometer.

2.5. Adsorption capability test of the prepared CMS- CoFe_2O_4 and pCMS- CoFe_2O_4 composites

In a universal bottle, 20 mg of the samples was immersed in 25 mL of RhB solution. The bottle was placed in a thermostatic shaker with water bath kept at 25°C . After a certain period of time,

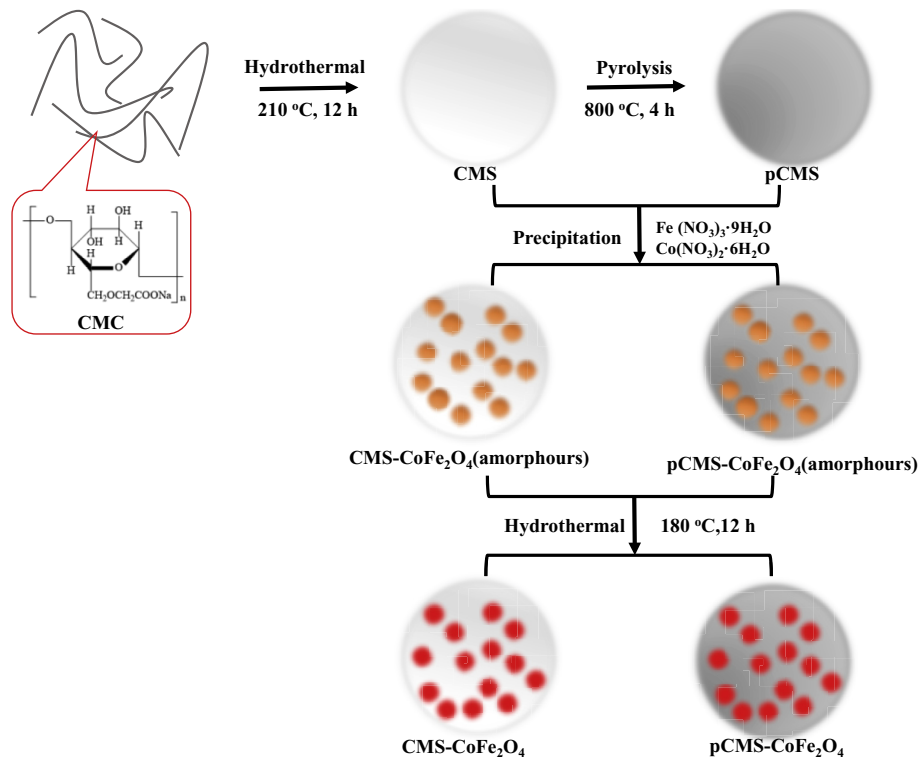


Fig. 1. Illustration of the formation of CMS-CoFe₂O₄ and pCMS-CoFe₂O₄.

the solution samples were taken out and the amount of the absorbed RhB by the prepared composites was determined by a UV–Vis spectroscopy. After measuring, the solutions were poured back into the bottle at once to keep the total volume of the solution constant. The RhB removal rate was calculated using the following equation:

$$\text{Removal, \%} = \frac{C_0 - C_t}{C_0} \times 100 \quad (1)$$

where C_0 is the initial RhB concentration (mg/L), C_t is the dye concentration at equilibrium (mg/L). Each absorption experiments were duplicated and the average value was adopted.

2.6. Photocatalytic activities measurement of the prepared CMS-CoFe₂O₄ and pCMS-CoFe₂O₄ composites

A tungsten halogen lamp with 500 W output power was used as the light source for the photocatalytic experiments and a water-jacketed quartz beaker was used as the reaction vessel, enabling a constant temperature of 28 ± 2 °C by adjusting the flow of cooling water.

In a typical photo-degradation process, exact 200 mL of RhB solution was prepared with predetermined concentrations in the quartz beaker. The photocatalyst of 50 mg was added into the RhB solution, and the mixture was then mechanically stirred in the dark for 30 min to achieve adsorption–desorption equilibrium. The quartz beaker with the mixtures of photocatalyst and RhB solution was then directly placed in front of the tungsten halogen lamp with a fixed distance of 20 cm. During the photocatalytic processes, approximate 3.0 mL of the mixture was withdrawn at predetermined time intervals, which was immediately centrifuged to separate the solid phase and the concentration of RhB was further quantified with the UV–vis spectrometer (Lambda-18 UV–visible

spectrometer). The absorbance wavelength of 665 nm was selected to analyze the concentration variation of the RhB solutions. The RhB solutions with initial concentration of 20 and 40 mg/L were diluted twice and four times before measurement by the UV–vis spectrometer. At each predetermined interval, the total organic carbon (TOC) of the degraded dye solution was analyzed by Shimadzu TOC-5000A analyzer.

3. Results and discussion

The structures of the prepared composites were first investigated. Fig. 2 shows the FT-IR spectra of CMS, pCMS, CMS-CoFe₂O₄ and pCMS-CoFe₂O₄. It can be seen from Fig. 2(a) that the CMS had a broad band at $\sim 3000\text{--}3500$ cm⁻¹, which was attributed to the stretching vibration of the –OH groups. The band at 1630 cm⁻¹, 1380 cm⁻¹ and 810 cm⁻¹ represented for the stretching vibration of the C=O groups, and the bending vibration of the C–H and the asymmetrical stretching vibration of the cyclic C–O–C, respectively. The spectrum of CMS indicated that the –OH groups still abundantly existed after the hydrothermal treatment (Sevilla and Fuertes, 2009). Meanwhile, Fig. 2(a) also showed that after a pyrolysis process, the band of the pCMS at $\sim 3000\text{--}3500$ cm⁻¹ became narrower and the intensity of the band at 1630 cm⁻¹ became weaker, indicating that the pyrolysis procedures removed a large amount of oxygen-containing groups on the carbon microspheres. It could also be observed that the two bands appearing at 1620 cm⁻¹ and 1538 cm⁻¹ were attributed to the characteristic peak of the benzene ring skeleton, which suggested that after the calcination procedure, the graphitic structure appeared in the prepared pCMS. Meanwhile, it could be seen from Fig. 2(b) that the band at 594 cm⁻¹ was attributed to the intrinsic stretching vibrations of metal oxygen bands at tetrahedral sub-lattices. The peaks at ~ 1244 cm⁻¹ and 1095 cm⁻¹ were due to the vibration of Fe–Co alloy system. The band at 1623 cm⁻¹ and 3000–3500 cm⁻¹ were the

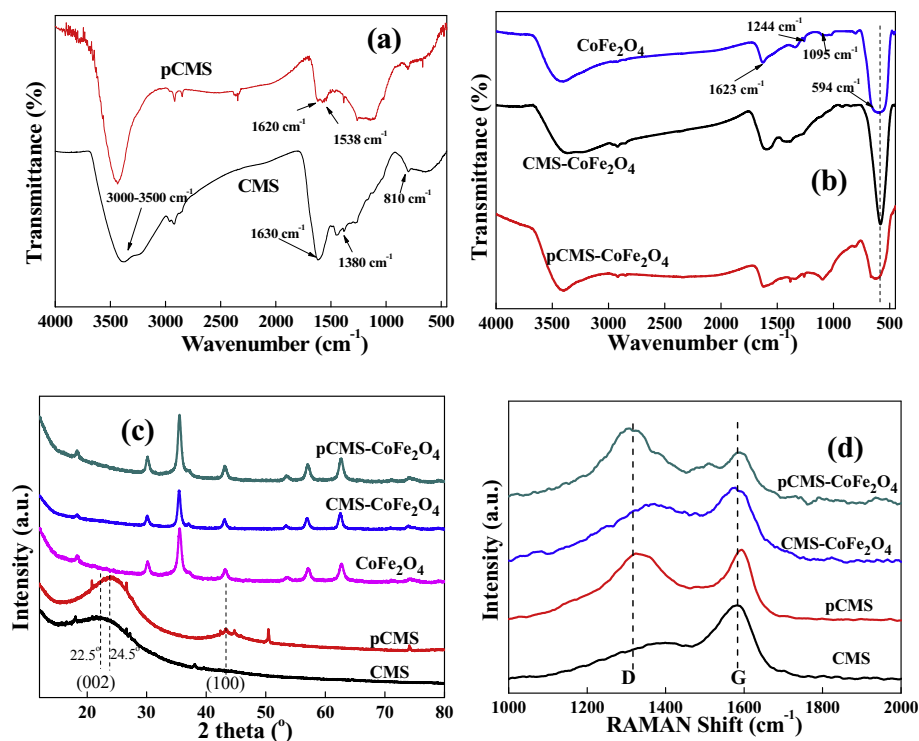


Fig. 2. FT-IR spectra of (a) CMS and pCMS, (b) pure CoFe₂O₄, CMS-CoFe₂O₄ and pCMS-CoFe₂O₄, (c) XRD patterns and (d) Raman spectra of CMS, pCMS, pure CoFe₂O₄, CMS-CoFe₂O₄ and pCMS-CoFe₂O₄.

bending and stretching vibration of the absorbed water, respectively (Rana et al., 2010). In addition, it was also observed that pure CoFe₂O₄, CMS-CoFe₂O₄ and pCMS-CoFe₂O₄ all exhibited similar spectra, indicating the incorporation of CMS and pCMS did not destroy the structure of the CoFe₂O₄ during the hydrothermal crystallization process of the CoFe₂O₄. Moreover, it was reported that the CoFe₂O₄ interacted with the carbonaceous materials through counter-ion interactions between the residual OH⁻ group from the carbonaceous materials and the Co²⁺ and Fe²⁺ ions from the CoFe₂O₄ (Li et al., 2011). It was also seen also seen from Fig. 2(b) that the peaks at 1623 cm⁻¹ and 3000-3500 cm⁻¹ both became broader, suggesting the interactions between CoFe₂O₄ nanoparticles and the CMS and pCMS.

Fig. 2(c) shows the XRD patterns of the CMS, pCMS, pure CoFe₂O₄, CMS-CoFe₂O₄ and pCMS-CoFe₂O₄. As could be seen, CMS demonstrated a wide peak at ~22.5°, which corresponded to the amorphous carbon. This meant that after a hydrothermal step, numerous oxygen-containing groups were removed and the carbon atoms in the cellulose skeleton turned to amorphous state (Kang et al., 2012). After the calcination step at 800 °C, the peak shifted to ~24.5°, accompanied by the appearance of a new peak at ~44°, which were the characteristic diffraction peaks of the d₀₀₂ and d₁₀₀ lattice plane of the graphite-structured carbon (Xia and Mokaya, 2004). Moreover, the d₀₀₂ peak intensity of the pCMS became sharper, indicating a higher graphitization degree. The results revealed that the high temperature calcination procedures could significantly increase the graphitic degree of the carbon microspheres, which was important for the photocatalytic properties of the following prepared composites.

It could also be seen from Fig. 2(c) that both CMS-CoFe₂O₄ and pCMS-CoFe₂O₄ had similar patterns with pure CoFe₂O₄, indicating that the incorporation of the carbon microspheres did not break the crystalline structure of the CoFe₂O₄. Since the amount of carbon microspheres in both CMS-CoFe₂O₄ and pCMS-CoFe₂O₄ was small,

it was difficult to observe the characteristic peaks of the carbon microspheres in the composite systems.

The existence status of the carbon microspheres could be further investigated using Raman spectroscopy. Fig. 2(d) shows the Raman spectra of CMS, pCMS, CMS-CoFe₂O₄ and pCMS-CoFe₂O₄. It is known that the graphitic materials have two characteristic peaks at ~1350 cm⁻¹ and 1680 cm⁻¹, which are generally named as the D band and G band (Gan et al., 2015b). The existence of the D band and G band is a direct evidence of the existence of the aromatic graphitic structure within the investigated material. Especially for biochar materials, the D band is assigned to ordered C-C between benzene rings and aromatics with six or more fused benzene rings, while G band represents for aromatic ring quadrant breathing (Azargohar et al., 2014). Moreover, the intensity ratio of these two bands (I_D/I_G) is often introduced to distinguish the graphitic degree. The increase in I_D/I_G value often indicates increased number of aromatic rings in the materials system. It could be clearly seen from Fig. 2(d) that both CMS and CMS-CoFe₂O₄ had a strong G band peak and nearly no D band peak was observed, indicating that the graphitic degree of the CMS was relatively low after only a hydrothermal treatment. Comparatively, both D band and G band peaks of the pCMS and pCMS-CoFe₂O₄ were very strong, and the I_D/I_G value increased significantly to 0.92 (Cai et al., 2014). This meant that more fused benzene rings were formed in the pCMS related materials after the pyrolysis process, which was in accordance with the XRD results illustrated above. It is also known that the I_D/I_G is also used to distinguish the structural defect. It could be observed from Fig. 2(d) that the I_D/I_G value of the pCMS-CoFe₂O₄ (I_D/I_G = 1.31) was higher than that of pCMS (I_D/I_G = 0.92). This meant during the hydrothermal formation of the CoFe₂O₄ crystalline structure, more residual cellulose functional groups on the pCMS were removed (Eigler et al., 2012). Besides, some CoFe₂O₄ molecules interacted with the pCMS, resulting in the formation of some structural defects of the obtained pCMS-CoFe₂O₄.

The surface chemical composition of the CMS and pCMS was further investigated by XPS with the results shown in Fig. 3. Carbon (C_{1s} at 284–289 eV) and oxygen (O_{1s} at 531–535 eV) elements were identified in both samples. As could be seen, both CMS and pCMS had carbon and oxygen containing groups. Moreover, carbon content increased after the pyrolysis treatment, in which the C/O ratio increased from 80/20 (CMS) to 85/15 (pCMS). The integrated results indicated that a further pyrolysis step could brought about more amorphous carbon with graphitic structures to the carbon microsphere structure.

The morphology of the composites was further observed by SEM with the results shown in Fig. 4. As could be seen from Fig. 4(a), pure $CoFe_2O_4$ had a nano-sphered structure in which the nano-sized particles were assembled together. It could also be seen from Fig. 4(b) and (c) that when the carbon microspheres were introduced, both CMS- $CoFe_2O_4$ and pCMS- $CoFe_2O_4$ represented composite structure in which the spherical CMS and pCMS were randomly dispersed within the $CoFe_2O_4$ nanoparticles. Since the CMS and pCMS were micrometer sized and the incorporation amount was relatively small, the $CoFe_2O_4$ agglomerates be could still observed. The magnified image as shown in Fig. 4(d) provided clear evidence that some of the $CoFe_2O_4$ nanoparticles were loaded on the surface of the carbon microspheres. Moreover, the elemental composition of the hybrid was examined by EDS spectroscopy with the results shown in Fig. 4(e). It could be seen that the atomic ratio of Co/Fe was $\sim 1/2$, very close to the stoichiometric ratio of $CoFe_2O_4$. This suggested the successful synthesis of spinel $CoFe_2O_4$ on the surface of the carbon microspheres, which was in accordance with the XRD results.

The DRS spectra of the pure $CoFe_2O_4$, CMS- $CoFe_2O_4$ and pCMS- $CoFe_2O_4$ were shown in Fig. 5(a). As could be seen, all three photocatalysts were responsive to the whole range of testing light. Pure $CoFe_2O_4$ had relatively high absorption capability in the UV region, and when the wavelength of the incident light increased to higher

than 500 nm, the absorbance decreased significantly. Since the CMS was not fully graphitized, the CMS had limited capability to influence the absorption efficiency of $CoFe_2O_4$. Comparatively, it could be clearly observed that the pCMS- $CoFe_2O_4$ had much higher absorption efficiency than pure $CoFe_2O_4$, and CMS- $CoFe_2O_4$, especially in visible light range. It is well known that the graphitic carbon materials possess strong absorption capability of light from UV to visible light regions. Thus the introduction of the pCMS significantly enhance the light absorption rate due to the abundant existence of the graphitic structure within the pCMS skeleton. Moreover, the inset image shows the band gap energy (E_g) transferred from Kubelka–Munk function. As could be observed, pure $CoFe_2O_4$ had a band gap of 1.28 eV, which was close to the previous studies (Gan et al., 2016a). The introduction of carbon microspheres could reduce the band gap energy of the pristine $CoFe_2O_4$, in which the CMS- $CoFe_2O_4$ had a band gap of 1.06 eV and pCMS- $CoFe_2O_4$ had a band gap of 0.87 eV. Accompanied with the results of the light absorption range, it was noted that pCMS could enhance the light absorption capability and narrow the band gap energy of the $CoFe_2O_4$ more significantly. Narrowed band gap energy could promote the separation efficiency of photogenerated electron–hole pairs and enhance the quantum yield of the photocatalyst, which was beneficial to the following RhB degradation efficiency.

Since the graphitic structure of the composites could significantly influence the photo-separation efficiency of the electron–hole pairs, the PL spectra of pure $CoFe_2O_4$, CMS- $CoFe_2O_4$ and pCMS- $CoFe_2O_4$ were conducted with the results shown in Fig. 5(b). It could be seen that the emission intensities of both CMS- $CoFe_2O_4$ and pCMS- $CoFe_2O_4$ were lower than that of pure $CoFe_2O_4$, indicating that the incorporation of carbon microspheres effectively inhibited the recombination of the excited electrons in the conduction band and the holes in the valence band. Meanwhile, it could also be observed that the emission intensity of the pCMS- $CoFe_2O_4$ was much lower compared to that of the CMS- $CoFe_2O_4$,

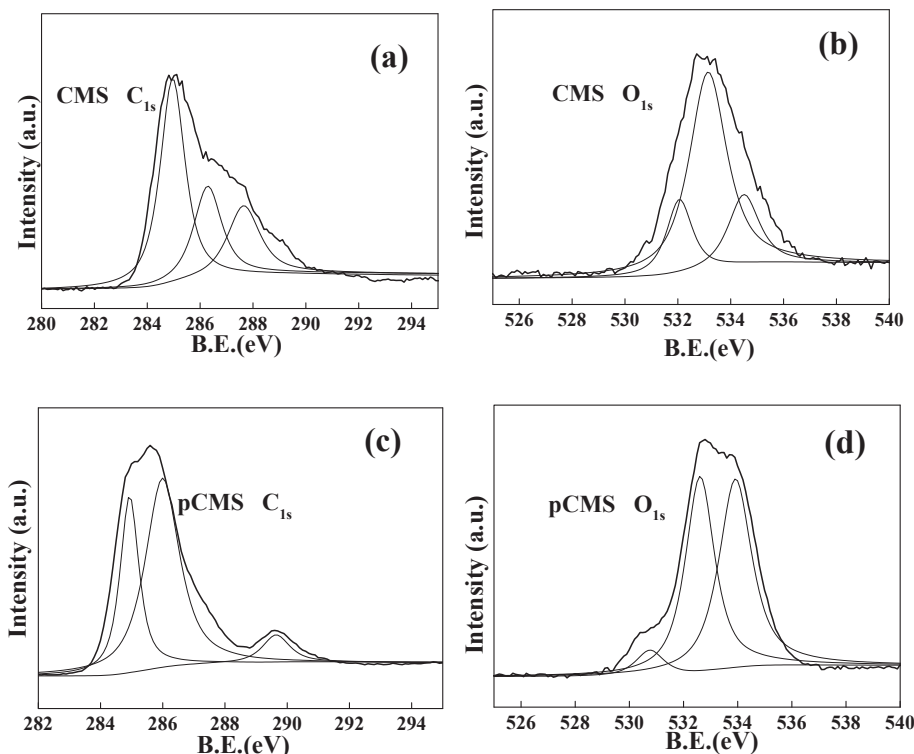


Fig. 3. High resolution XPS spectra of C_{1s} and O_{1s} in CMS and pCMS.

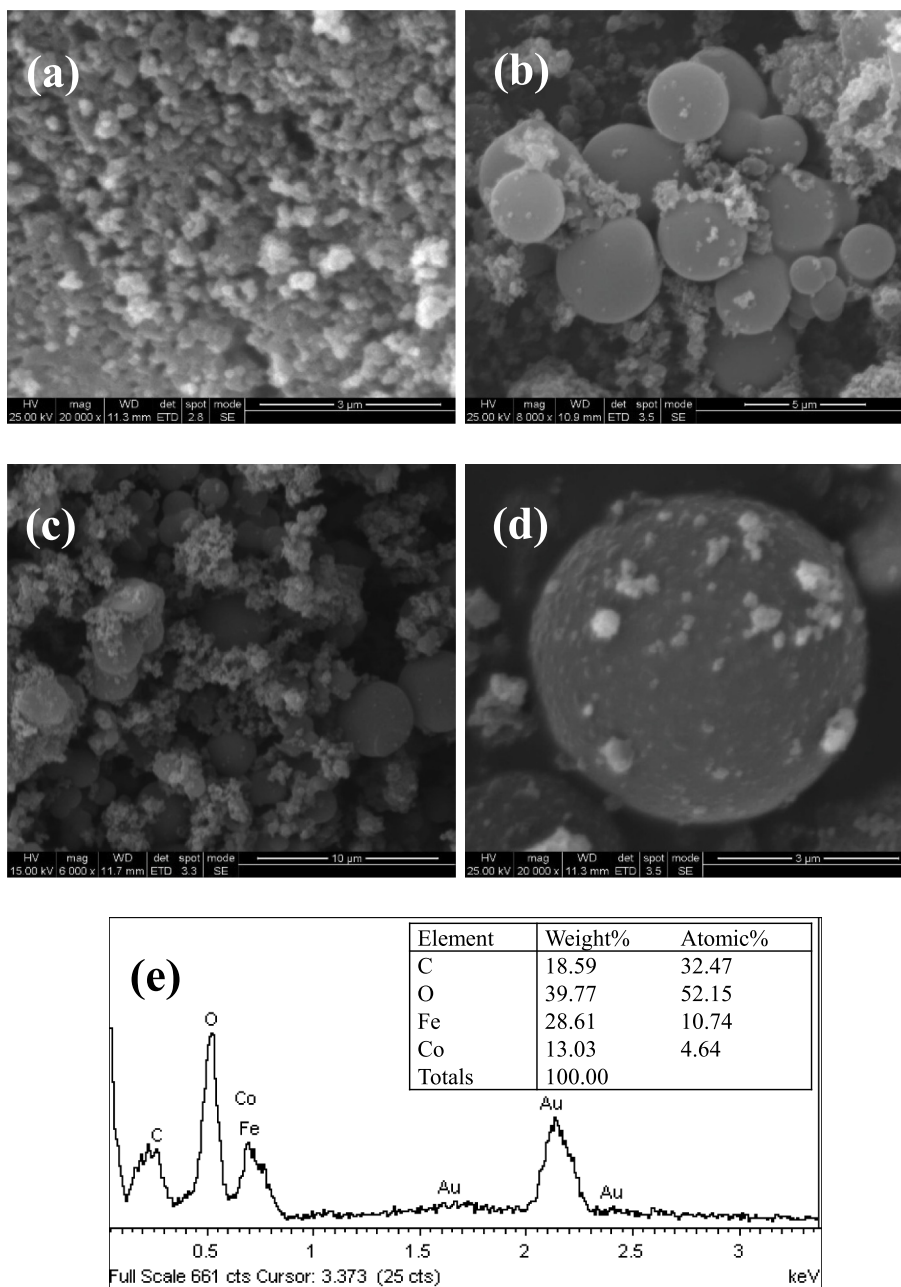


Fig. 4. SEM images of (a) pure CoFe_2O_4 (b) $\text{CMS-CoFe}_2\text{O}_4$, (c) $\text{pCMS-CoFe}_2\text{O}_4$, (d) magnified $\text{pCMS-CoFe}_2\text{O}_4$ and (e) EDS spectra of $\text{pCMS-CoFe}_2\text{O}_4$.

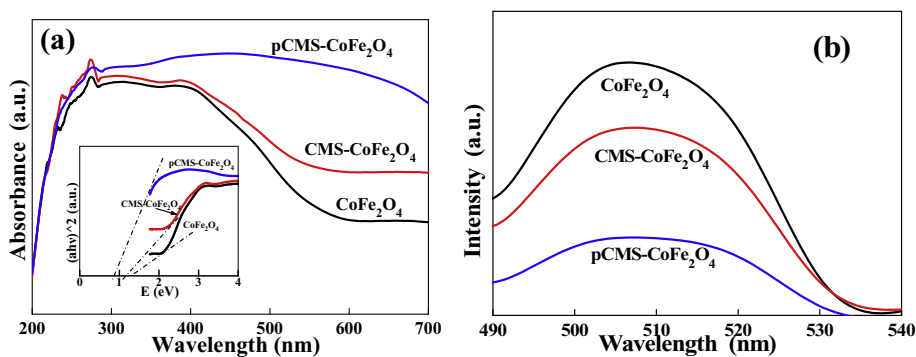


Fig. 5. (a) DRS spectra and (b) PL figures of pure CoFe_2O_4 , $\text{CMS-CoFe}_2\text{O}_4$ and $\text{pCMS-CoFe}_2\text{O}_4$.

which meant the excessive graphitic structure in the pCMS could trap the excited electrons and prolonged the lifetime of the holes more effectively.

Fig. 6(a) shows the nitrogen adsorption/desorption isotherms of the CMS and pCMS. It could be seen that both CMS and pCMS exhibited type I isotherms. Compared with that of the CMS, the adsorbed nitrogen of the pCMS enhance dramatically with the BET surface areas increased from 40 m²/g to 700 m²/g, indicating that the pyrolysis process brought about more pores and surface areas to the carbon microspheres.

The pore properties of the nanocomposites could be further investigated through adsorbing RhB dye with the results shown in Fig. 6(b). It could be seen that the adsorption capability of pure CoFe₂O₄ was poor due to limited pore structure and active sites. On the contrary, both CMS and pCMS showed promising adsorption performance since they both had pore structures. Since the high pyrolysis temperature resulted in more pores, the pCMS had better adsorption capability than that of CMS, which was in accordance with the above results. Moreover, since the pyrolysis process also created more graphitic and aromatic structures to pCMS, the pCMS could have abundant active groups to adsorb more RhB molecules through π - π and p- π conjugations. Comparatively, CMS-CoFe₂O₄ and pCMS-CoFe₂O₄ showed weaker adsorption capability due to limited mass contents of the CMS and pCMS in the composite systems. Additionally, the CoFe₂O₄ loaded on the carbon microsphere surface interfered the adhesion between CMS and RhB as well. However, due to the existence of the carbon microspheres, the adsorption performance of both CMS-CoFe₂O₄ and pCMS-CoFe₂O₄ was significantly improved compared with pure CoFe₂O₄. This was also critical for the subsequent photocatalytic process since the photocatalytic degradation of organic pollutants mainly happened on the surface of the photocatalysts and only the adsorbed molecules could participate in the reactions.

The photocatalytic performance of the prepared composites was then investigated by using RhB as a model pollutant, and the results were shown in Fig. 7(a). The RhB concentration was set at 10 mg/L and the composites dosage was 50 mg. For comparison, the performance of P25 under same condition was also examined. Since P25 only had a band gap of ~3.2 eV, it was only responsive under UV light irradiation. The wavelength range of the halogen-tungsten light was 380–820 nm, and therefore RhB could be hardly degraded by P25 under the irradiation of halogen-tungsten light. Pure CoFe₂O₄ could degrade no more than 30% of the RhB within the total reaction time. Conversely, both CMS-CoFe₂O₄ and pCMS-CoFe₂O₄ demonstrated much higher degradation rates. Particularly, the pCMS-CoFe₂O₄ could achieve entire degradation of RhB within 2 h. Meanwhile, the degradation capability of the CMS-CoFe₂O₄ was relatively low, in which the CMS-CoFe₂O₄ could only degrade ~70% of the RhB even the reaction time was prolonged to 3 h or longer.

The corresponding TOC removal during the dye degradation process was also investigated with the results shown in Fig. 7(b). In accordance with the photo-degradation results, the highest TOC removal rate was obtained when the pCMS-CoFe₂O₄ was used as the photocatalyst. Comparatively, pure CoFe₂O₄ and CMS-CoFe₂O₄ could only remove only ~10% and 30% of the TOC, respectively. It should also be pointed out that compared with the dye decoloration rate, the TOC removal proportion was relatively low. This meant the RhB molecules were not totally converted to inorganic molecules during the whole photo-degradation process.

The impact of dye concentration on the performance of the photocatalyst was then conducted with the results shown in Fig. 8(a). The composite of pCMS-CoFe₂O₄ was selected as the catalyst sample due to its optimum photocatalytic performance and the dosage was still 50 mg. As could be observed, when the RhB concentration was 20 mg/L or lower, 50 mg of the pCMS-CoFe₂O₄ could reach a complete degradation of RhB within 3.0 h. Meanwhile, when the RhB concentration reached to 30 mg/L, the pCMS-CoFe₂O₄ could not degrade all the dye molecules in 3 h. This might be attributed to the darker color of the concentrated dye solution which inhibited the contact between the incident light and the photocatalyst particles.

In the photocatalytic process, solution pH was found crucial which could influence the photocatalytic properties of a photocatalyst. Thus, the RhB degradation efficiency by using pCMS-CoFe₂O₄ as a function of pH is illustrated in Fig. 8(b). The experiments were conducted by dosing 50 mg of pCMS-CoFe₂O₄ into 100 mL of 10 mg/L RhB dye solution. As could be seen, weak acid condition was beneficial to RhB degradation. Since RhB is a weak basic dye, the RhB molecules are more inclined to attach onto the photocatalyst surface with moderate amount of H⁺. When the pH value increased as high as 11, the photo-degradation efficiency decreased dramatically, which was because excessive OH⁻ hindered the contact between the RhB and the photocatalyst. The results indicated that the prepared pCMS-CoFe₂O₄ photocatalyst was applicable in a wide range of pH values from 3 to 9.

With the CoFe₂O₄ present in the photocatalysts, the prepared composites were endowed with magnetism, which made the photocatalyst magnetically separable from the treated wastewater after the degradation process. Fig. 8(c) shows the hysteresis loop of the pCMS-CoFe₂O₄. It was noted that the pCMS-CoFe₂O₄ demonstrated strong magnetic quality with the saturation magnetization determined to be 63.5 emu/g. The pCMS-CoFe₂O₄ composite with strong magnetization could be easily separated with a magnet after the photo-degradation process (inset image of Fig. 8(c)), achieving the goal of cleaner production by preventing secondary pollution to the wastewater. With this property, the separated photocatalyst could be recycled for more degradation circles. Fig. 8(d) shows the recycled stability of the pCMS-CoFe₂O₄ in the degradation of RhB

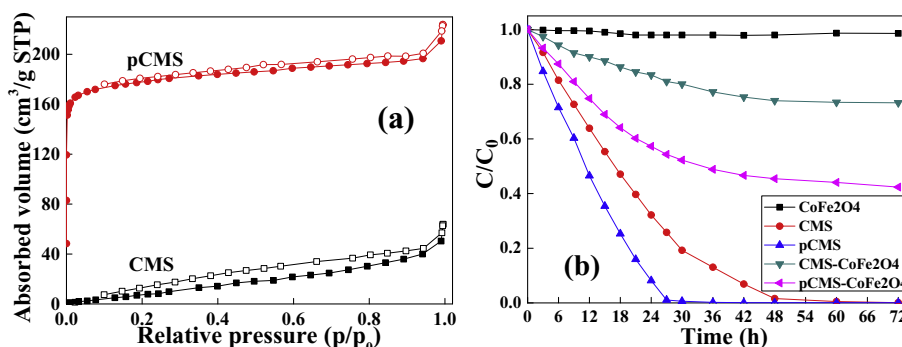


Fig. 6. (a) Nitrogen adsorption isotherm of CMS and pCMS, (b) Dye adsorption behavior of CMS, pCMS, pure CoFe₂O₄, CMS-CoFe₂O₄ and pCMS-CoFe₂O₄.

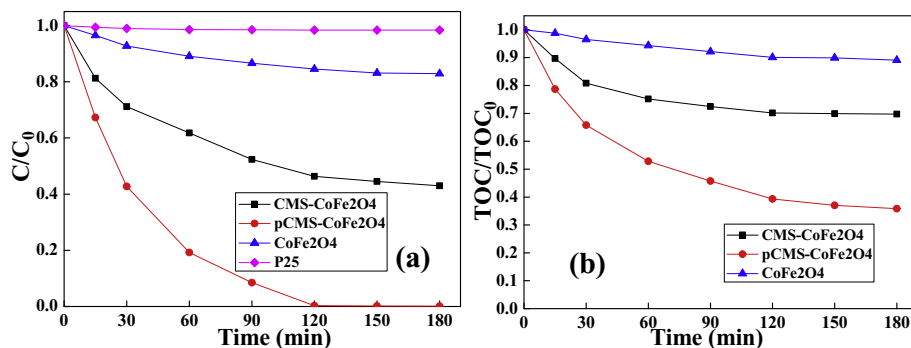


Fig. 7. (a) Photocatalytic degradation of RhB of the photocatalysts, and (b) TOC removal during the degradation process.

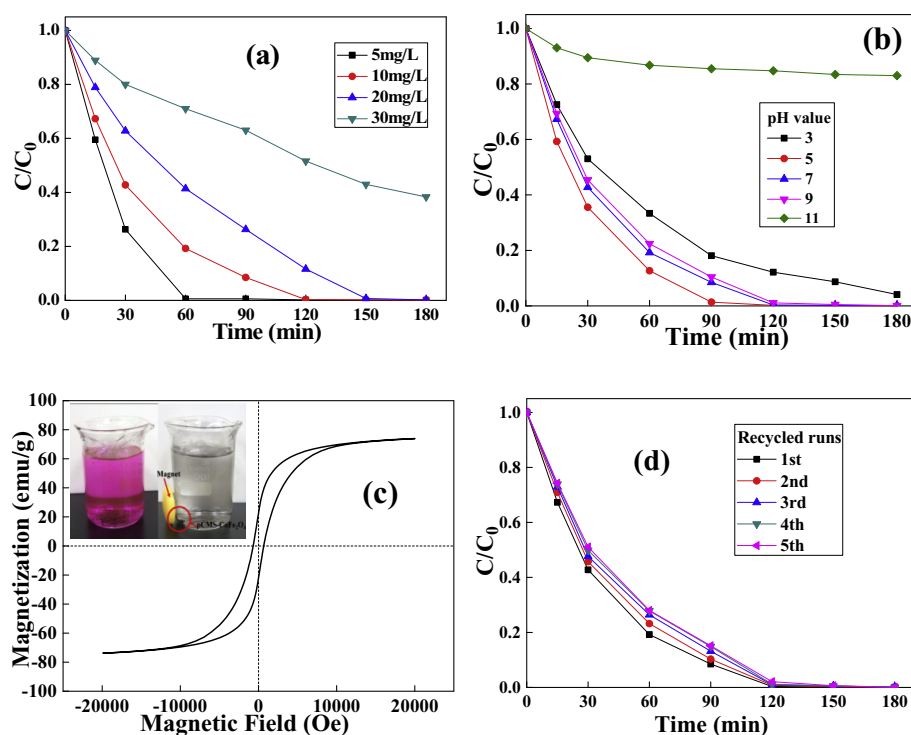


Fig. 8. Impact of (a) RhB concentration and (b) pH value on the degradation performance of pCMS-CoFe₂O₄, (c) hysteresis loop of pCMS-CoFe₂O₄ (inset: digital picture of the dye solutions before and after degradation) and (d) recycled performance of the pCMS-CoFe₂O₄ in degrading RhB (10 mg/L).

for five consecutive runs. The photo-degradation efficiency of the pCMS-CoFe₂O₄ was still very promising after five runs, although a slight decrease was observed due to the adsorption of the dye molecules on the pCMS surface. This indicated that the prepared pCMS-CoFe₂O₄ had very desirable photo-degradation stability which was environmental sustainable and recyclable for many times.

Based on the above overall results, a photo-degradation mechanism of the CoFe₂O₄ loaded carbon microspheres was proposed in Fig. 9. Generally, continuous light irradiation excited the electrons from the valence band (VB) to the conduction band (CB), and the holes in the CB then captured the electrons from the H₂O/OH⁻ and form reactive [•]OH radicals. The reactive [•]OH radicals generated redox reactions degraded RhB molecules afterwards (Li et al., 2013). Since the excited electrons are highly unstable, they are inclined to go back to CB and recombine with the holes. Thus the key to improve the photo-degradation efficiency of the photocatalyst was to postpone the recombination of the electrons and holes,

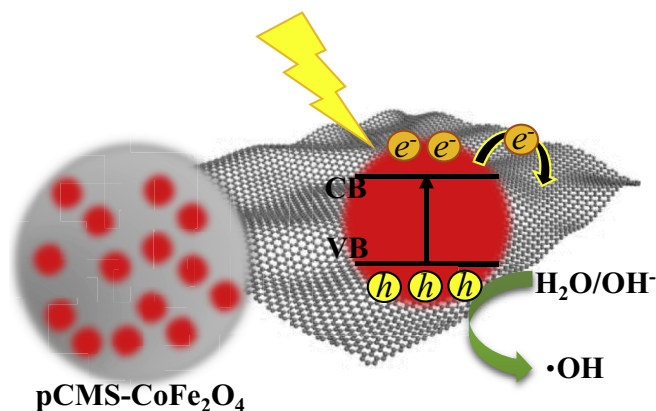


Fig. 9. Proposed mechanism of the photocatalysis process.

providing higher opportunities for the holes to generate $\cdot\text{OH}$ radicals (Zhu et al., 2011). With the carbon microsphere in the photocatalyst system, the pore structures of the CMS and pCMS could adsorb RhB molecules around the CoFe_2O_4 , the generated $\cdot\text{OH}$ radicals could contact and degrade RhB molecules more quickly than that of pure CoFe_2O_4 , as discussed above. Moreover, the graphitic and aromatic structures of the carbon microspheres could trap and stabilize the excited electrons, hindering the recombination of the electrons and the holes. Since the aromatization and the graphitization degree of the pCMS was higher, the pCMS- CoFe_2O_4 thus had higher photocatalytic efficiency.

4. Conclusions

In summary, the bio-renewable and magnetically recyclable photocatalysts based on cellulose derived CMS- CoFe_2O_4 and pCMS- CoFe_2O_4 composites were fabricated in the present study. The photocatalytic properties of the prepared composites were then investigated by using RhB as a model pollutant. Compared with pure CoFe_2O_4 , the CMS- CoFe_2O_4 and pCMS- CoFe_2O_4 showed much better photocatalytic performance. Since the pyrolysis process brought about more pores and higher graphitization degree to pCMS, the pCMS- CoFe_2O_4 had better photocatalytic performance. Moreover, the prepared composites could be magnetically separated from the wastewater and showed promising recycle stability. This study not only provides a promising recyclable photocatalyst which could be potentially applied in water purification, but also provide a novel idea for applying bio-renewable biomass derived materials in the field of sustainable wastewater treatment.

Acknowledgements

This work was supported by Natural Science Foundation of Jiangsu Province, China (BK20160938, BK20160936), Natural Science Foundation of China (51708297), Scientific Research Foundation for High-level Talents of Nanjing Forestry University (GXL2016021), Top-notch Academic Programs Project of Jiangsu Higher Education Institutions (TAPP), the Priority Academic Program Development of Jiangsu Higher Education Institutions (PAPD).

References

- Achouri, F., Corbel, S., Balan, L., Mozet, K., Giro, E., Medjahdi, G., Said, M.B., Ghrabi, A., Schneider, R., 2016. Porous Mn-doped ZnO nanoparticles for enhanced solar and visible light photocatalysis. *Mater. Des.* 101, 309–316.
- Ahmad, M., Ahmed, E., Hong, Z.L., Xu, J.F., Khalid, N.R., Elhissi, A., Ahmed, W., 2013. A facile one-step approach to synthesizing ZnO/graphene composites for enhanced degradation of methylene blue under visible light. *Appl. Surf. Sci.* 274, 273–281.
- Ananpattarachai, J., Kajitvichyanukul, P., 2016. Enhancement of chromium removal efficiency on adsorption and photocatalytic reduction using a bio-catalyst, titania-impregnated chitosan/xylan hybrid film. *J. Clean. Prod.* 130, 126–136.
- Ao, Y., Tang, H., Wang, P., Wang, C., Hou, J., Qian, J., 2014. Synthesis, characterization and photocatalytic activity of $\text{BiOBr}-\text{AC}$ composite photocatalyst. *Compos. B Eng.* 59, 96–100.
- Azargohar, R., Nanda, S., Kozinski, J.A., Dalai, A.K., Surtaro, R., 2014. Effects of temperature on the physicochemical characteristics of fast pyrolysis bio-chars derived from Canadian waste biomass. *Fuel* 125, 90–100.
- Cai, Y., Wang, Y., Deng, S., Chen, G., Li, Q., Han, B., Han, R., Wang, Y., 2014. Graphene nanosheets-tungsten oxides composite for supercapacitor electrode. *Ceram. Int.* 40, 4109–4116.
- Choi, Y.I., Kim, Y.-I., Cho, D.W., Kang, J.-S., Leung, K.T., Sohn, Y., 2015. Recyclable magnetic $\text{CoFe}_2\text{O}_4/\text{BiOx}$ ($X = \text{Cl}, \text{Br}$ and I) microflowers for photocatalytic treatment of water contaminated with methyl orange, rhodamine B, methylene blue, and a mixed dye. *RSC Adv.* 5, 79624–79634.
- Della Pina, C., Ferretti, A.M., Ponti, A., Falletta, E., 2015. A green approach to magnetically-hard electrically-conducting polyaniline/ CoFe_2O_4 nanocomposites. *Compos. Sci. Technol.* 110, 138–144.
- Dhiman, P., Naushad, M., Batoo, K.M., Kumar, A., Sharma, G., Ghfar, A.A., Kumar, G., Singh, M., 2017. Nano $\text{Fe}_x\text{Zn}_{1-x}\text{O}$ as a tuneable and efficient photocatalyst for solar powered degradation of bisphenol A from aqueous environment. *J. Clean. Prod.* 165, 1542–1556.
- Dunnigan, L., Ashman, P.J., Zhang, X., Kwong, C.W., 2018. Production of biochar from rice husk: particulate emissions from the combustion of raw pyrolysis volatiles. *J. Clean. Prod.* 172, 1639–1645.
- Eigler, S., Dotzer, C., Hirsch, A., 2012. Visualization of defect densities in reduced graphene oxide. *Carbon* 50, 3666–3673.
- Fu, Y., Chen, H., Sun, X., Wang, X., 2012. Combination of cobalt ferrite and graphene: high-performance and recyclable visible-light photocatalysis. *Appl. Catal. B Environ.* 111–112, 280–287.
- Gan, L., Shang, S., Yuen, C.W.M., Jiang, S.-x., Hu, E., 2015a. Hydrothermal synthesis of magnetic CoFe_2O_4 /graphene nanocomposites with improved photocatalytic activity. *Appl. Surf. Sci.* 351, 140–147.
- Gan, L., Shang, S.M., Yuen, C.W.M., Jiang, S.X., 2015b. Covalently functionalized graphene with d-glucose and its reinforcement to poly(vinyl alcohol) and poly(methyl methacrylate). *RSC Adv.* 5, 15954–15961.
- Gan, L., Xu, L., Qian, K., 2016a. Preparation of core-shell structured CoFe_2O_4 incorporated Ag_3PO_4 nanocomposites for photocatalytic degradation of organic dyes. *Mater. Des.* 109, 354–360.
- Gan, L., Xu, L., Shang, S., Zhou, X., Meng, L., 2016b. Visible light induced methylene blue dye degradation photo-catalyzed by WO_3 /graphene nanocomposites and the mechanism. *Ceram. Int.* 42, 15235–15241.
- Hadnadjev-Kostic, M., Vulic, T., Marinkovic-Neducin, R., Lončarević, D., Dostanić, J., Markov, S., Jovanović, D., 2017. Photo-induced properties of photocatalysts: a study on the modified structural, optical and textural properties of TiO_2-ZnAl layered double hydroxide based materials. *J. Clean. Prod.* 164, 1–18.
- Hassan, M., Haque, E., Reddy, K.R., Minett, A.L., Chen, J., Gomes, V.G., 2014. Edge-enriched graphene quantum dots for enhanced photo-luminescence and supercapacitance. *Nanoscale* 6, 11988–11994.
- Hu, J., Men, J., Liu, Y., Huang, H., Jiao, T., 2015. One-pot synthesis of Ag-modified LaMnO_3 -graphene hybrid photocatalysts and application in the photocatalytic discoloration of an azo-dye. *RSC Adv.* 5, 54028–54036.
- Kang, S., Li, X., Fan, J., Chang, J., 2012. Characterization of hydrochars produced by hydrothermal carbonization of lignin, cellulose, D-xylose, and wood meal. *Ind. Eng. Chem. Res.* 51, 9023–9031.
- Laadila, M.A., Hegde, K., Rouissi, T., Brar, S.K., Galvez, R., Sorelli, L., Cheikh, R.B., Paiva, M., Abokitse, K., 2017. Green synthesis of novel biocomposites from treated cellulosic fibers and recycled bio-plastic polylactic acid. *J. Clean. Prod.* 164, 575–586.
- Li, N., Zheng, M., Chang, X., Ji, G., Lu, H., Xue, L., Pan, L., Cao, J., 2011. Preparation of magnetic CoFe_2O_4 -functionalized graphene sheets via a facile hydrothermal method and their adsorption properties. *J. Solid State Chem.* 184, 953–958.
- Li, Z.X., Shen, Y., Yang, C., Lei, Y.C., Guan, Y.H., Lin, Y.H., Liu, D.B., Nan, W., 2013. Significant enhancement in the visible light photocatalytic properties of BiFeO_3 -graphene nanohybrids. *J. Mater. Chem. A* 1, 823–829.
- Meng, S., Li, D., Wang, P., Zheng, X., Wang, J., Chen, J., Fang, J., Fu, X., 2013. Probing photonic effect on photocatalytic degradation of dyes based on 3D inverse opal ZnO photonic crystal. *RSC Adv.* 3, 17021–17028.
- Pi, L., Jiang, R., Zhou, W., Zhu, H., Xiao, W., Wang, D., Mao, X., 2015. g-C $_3$ N $_4$ Modified biochar as an adsorptive and photocatalytic material for decontamination of aqueous organic pollutants. *Appl. Surf. Sci.* 358, 231–239.
- Pozo-Antonio, J.S., Dionísio, A., 2017. Self-cleaning property of mortars with TiO_2 addition using real diesel exhaust soot. *J. Clean. Prod.* 161, 850–859.
- Priyadharan, A., Vasanthakumar, V., Karthikeyan, S., Raj, V., Shanavas, S., Anbarasan, P.M., 2017. Multi-functional properties of ternary $\text{CeO}_2/\text{SnO}_2/\text{rGO}$ nanocomposites: visible light driven photocatalyst and heavy metal removal. *J. Photochem. Photobiol., A* 346, 32–45.
- Rana, S., Philip, J., Raj, B., 2010. Micelle based synthesis of cobalt ferrite nanoparticles and its characterization using Fourier Transform infrared transmission spectrometry and thermogravimetry. *Mater. Chem. Phys.* 124, 264–269.
- Reddy, K.R., Gomes, V.G., Hassan, M., 2014. Carbon functionalized TiO_2 nanofibers for high efficiency photocatalysis. *Mater. Res. Express* 1, 015012.
- Reddy, K.R., Hassan, M., Gomes, V.G., 2015. Hybrid nanostructures based on titanium dioxide for enhanced photocatalysis. *Appl. Catal. A Gen.* 489, 1–16.
- Reddy, K.R., Karthik, K.V., Prasad, S.B.B., Soni, S.K., Jeong, H.M., Raghav, A.V., 2016. Enhanced photocatalytic activity of nanostructured titanium dioxide/polyaniline hybrid photocatalysts. *Polyhedron* 120, 169–174.
- Reddy, K.R., Lee, K.P., Gopalan, A.I., 2008a. Self-assembly approach for the synthesis of electro-magnetic functionalized Fe_3O_4 /polyaniline nanocomposites: effect of dopant on the properties. *Colloid. Surf. A* 320, 49–56.
- Reddy, K.R., Nakata, K., Ochiai, T., Murakami, T., Tryk, D.A., Fujishima, A., 2011. Facile fabrication and photocatalytic application of Ag nanoparticles- TiO_2 nanofiber composites. *J. Nanosci. Nanotechnol.* 11, 3692–3695.
- Reddy, K.R., Sin, B.C., Yoo, C.H., Park, W., Ryu, K.S., Lee, J.-S., Sohn, D., Lee, Y., 2008b. A new one-step synthesis method for coating multi-walled carbon nanotubes with cuprous oxide nanoparticles. *Scripta Mater.* 58, 1010–1013.
- Sevilla, M., Fuenes, A.B., 2009. The production of carbon materials by hydrothermal carbonization of cellulose. *Carbon* 47, 2281–2289.
- Wan, C., Lu, Y., Jiao, Y., Jin, C., Sun, Q., Li, J., 2015. Fabrication of hydrophobic, electrically conductive and flame-resistant carbon aerogels by pyrolysis of regenerated cellulose aerogels. *Carbohydr. Polym.* 118, 115–118.
- Wang, Y., Wang, H., Chen, F., Cao, F., Zhao, X., Meng, S., Cui, Y., 2017. Facile synthesis of oxygen doped carbon nitride hollow microsphere for photocatalysis. *Appl. Catal. B Environ.* 206, 417–425.
- Wu, Q., Li, W., Tan, J., Nan, X., Liu, S., 2015a. Hydrothermal synthesis of magnetic mesoporous carbon microspheres from carboxymethylcellulose and nickel acetate. *Appl. Surf. Sci.* 332, 354–361.

- Wu, Q., Li, W., Tan, J., Wu, Y., Liu, S., 2015b. Hydrothermal carbonization of carboxymethylcellulose: one-pot preparation of conductive carbon microspheres and water-soluble fluorescent carbon nanodots. *Chem. Eng. J.* 266, 112–120.
- Xia, Y., Mokaya, R., 2004. Synthesis of ordered mesoporous carbon and nitrogen-doped carbon materials with graphitic pore walls via a simple chemical vapor deposition method. *Adv. Mater.* 16, 1553–1558.
- Xu, L., Wang, Y., Liu, J., Han, S., Pan, Z., Gan, L., 2017. High-efficient visible-light photocatalyst based on graphene incorporated Ag₃PO₄ nanocomposite applicable for the degradation of a wide variety of dyes. *J. Photochem. Photobiol., A* 340, 70–79.
- Zhu, M.S., Chen, P.L., Liu, M.H., 2011. Graphene oxide enwrapped Ag/AgX (X = Br, Cl) nanocomposite as a highly efficient visible-light plasmonic photocatalyst. *ACS Nano* 5, 4529–4536.